Received: 18 September 2022 | Revised: 1 October 2023 | Accepted: 6 October 2023

DOI: 10.1002/we.2877

SPECIAL ISSUE PAPER

WILEY

Profiling wind LiDAR measurements to quantify blockage for onshore wind turbines

Coleman Moss[1] | Matteo Puccioni[1] | Romit Maulik[2] | Clément Jacquet[3] | Dale Apgar[3] | Giacomo Valerio Iungo[1]

[1]Department of Mechanical Engineering, Center for Wind Energy, Wind Fluids and Experiments (WindFluX) Laboratory, The University of Texas at Dallas, Dallas, Texas, USA

[2]Argonne National Laboratory, Lemont, Illinois, USA

[3]General Electrics Renewables, Ponferrada, Spain

Correspondence
Giacomo Valerio Iungo, 800 West Campbell Rd, WT 10, Richardson, TX 75080-3021, USA.
Email: valerio.iungo@utdallas.edu

Funding information
Division of Chemical, Bioengineering, Environmental, and Transport Systems, Grant/Award Number: 2046160; National Science Foundation, Grant/Award Numbers: 1362022, 1362033, 1916715, 1916776

Abstract

Flow modifications induced by wind turbine rotors on the incoming atmospheric boundary layer (ABL), such as blockage and speedups, can be important factors affecting the power performance and annual energy production (AEP) of a wind farm. Further, these rotor-induced effects on the incoming ABL can vary significantly with the characteristics of the incoming wind, such as wind shear, veer, and turbulence intensity, and turbine operative conditions. To better characterize the complex flow physics underpinning the interaction between turbine rotors and the ABL, a field campaign was performed by deploying profiling wind LiDARs both before and after the construction of an onshore wind turbine array. Considering that the magnitude of these rotor-induced flow modifications represents a small percentage of the incoming wind speed ($\approx 3\%$), high accuracy needs to be achieved for the analysis of the experimental data and generation of flow predictions. Further, flow distortions induced by the site topography and effects of the local climatology need to be quantified and differentiated from those induced by wind turbine rotors. To this aim, a suite of statistical and machine learning models, such as k-means cluster analysis coupled with random forest predictions, are used to quantify and predict flow modifications for different wind and atmospheric conditions. The experimental results show that wind velocity reductions of up to 3% can be observed at an upstream distance of 1.5 rotor diameter from the leading wind turbine rotor, with more significant effects occurring for larger positive wind shear. For more complex wind conditions, such as negative shear and low-level jet, the rotor induction becomes highly complex entailing either velocity reductions (down to 9%) below hub height and velocity increases (up to 3%) above hub height. The effects of the rotor induction on the incoming wind velocity field seem to be already roughly negligible at an upstream distance of three rotor diameters. The results from this field experiment will inform models to simulate wind-turbine and wind-farm operations with improved accuracy for flow predictions in the proximity of the rotor area, which will be instrumental for more accurate quantification of wind farm blockage and relative effects on AEP.

KEYWORDS
blockage, LiDAR, machine learning, wind farm

1 | INTRODUCTION

The atmospheric boundary layer (ABL) is the source of the power harvested by wind turbines. Thus, a detailed characterization of ABL features, for example, in terms of wind speed, wind direction, turbulence intensity, shear, and veer, is instrumental for the design of wind turbine rotor aerodynamics and controls as well as the optimization of wind farm layouts. With the increase in wind turbine size and with the deployment of wind farms encompassing a larger number of wind turbines, it has been recognized that mutual interactions arise between the pressure field induced by the wind turbine rotors and the incoming wind field. Specifically, rotor-induced effects on the incoming ABL can entail velocity reductions typically occurring in front of and approaching the turbine, which are referred to as induction zone for a single wind turbine[1,2] and blockage encompassing cumulative effects due to multiple wind turbines.[3–5] Rotor-induced effects can also consist of flow deflections and speedups as the incoming wind field partially circumvents the turbine rotor due to pressure field modifications associated with the thrust force exerted by the turbine rotor.[6] Speedup regions have been observed numerically and through wind tunnel experiments,[7–10] while extensive field experimental evidence is still lacking.[11,12]

Regarding wind farm blockage, the comparison of wind speed measurements recently performed at the Lillgrund offshore wind farm before and after the construction of the wind power plant highlighted a velocity decrease corresponding to a 2% reduction in annual energy production (AEP).[11] Wind measurements performed with light detection and ranging (LiDAR) instruments for an offshore wind farm identified a large variability in wind speed reduction based on atmospheric stability regime and operative conditions of the wind turbines,[12] with the extreme scenarios observed during stable atmospheric conditions leading to a velocity deficit of 4% of the freestream value at an upstream distance of 25 rotor diameters (D). For onshore wind farms, the analysis of wind data collected before and after the construction of a wind power plant provided evidence of wind farm blockage, which is quantified to be about 3.4% of the freestream velocity at an upstream distance of 2D, while reducing to 1.9% at 10D.[13]

Large-eddy simulations (LES) of a wind farm performed for different incoming wind shear with constant hub-height wind speed and turbulence intensity, TI, aimed at simulating different levels of atmospheric stability, showed that at an upstream distance of 2.5D from the leading wind turbine, the velocity reduction changed from 0.8% to 10% with increasing wind shear.[14] Effects of the atmospheric stability on wind farm blockage were also simulated by varying the ABL height, specifically by varying it from 300 m up to 500 m for the LES of an ideal wind turbine array.[15] The LES data indicated that the wind speed reduction ascribed to wind farm blockage reduced from 3% down to 1.25% at an upstream distance of 5D with increasing ABL height. Nonetheless, caution should be paid to the setup and analysis of numerical simulations aiming at investigating wind farm blockage. Indeed, a recent study showed significant variability in the estimates of wind turbine power capture for different levels of atmospheric stratification, that is, ABL height, wind shear, and veer, by varying numerical domain size and grid resolution of the numerical setup.[16]

Wind tunnel experiments with down-scaled wind turbine models can also be informative to investigate wind farm blockage. Wind speed reductions up to an upstream distance of 30D were measured through laboratory experiments.[17] Similar results were obtained in Segalini & Dahlberg 2020,[18] where blockage effects on a turbine row induced by a downstream turbine row can become negligible only for streamwise spacing larger than 30D, while wind farm blockage is estimated between 0.9% and 2.4% depending on wind turbine density over the array and number of the wind turbine rows.

The challenges associated with investigations of mutual interactions between wind turbine rotors and the incoming wind field are connected with the three-dimensionality and the non-stationarity of the ABL,[19–21] and the variability in the settings of the wind turbine rotor, which leads to different turbine thrust and power coefficients, and, thus, wake velocity fields.[22–24] Further, the order of magnitude of the flow modifications caused by the rotor-induced effects is typically only a few percent of the freestream velocity. This is comparable to the variations in the freestream flow that can arise from terrain effects, complex atmospheric features, and statistical uncertainty associated with the measurements. Therefore, performing a thorough characterization of the site flow conditions and climatology is instrumental to the subsequent quantification of wind farm blockage and speed up from site-specific flow patterns.

In this work, we investigate the effects induced by wind turbine rotors on the incoming ABL for different wind and atmospheric conditions, and, more specifically, for different levels of shear (either positive or negative shear) and during the occurrence of low-level jets as well. This study is performed through a field experiment encompassing wind LiDAR profile measurements collected before and after the construction of an onshore wind turbine array to differentiate the spatial wind field variability due to the site topography for different wind/atmospheric conditions from the subtle effects on the incoming ABL associated with the rotor thrust force. To identify these rotor-induced effects, meticulous procedures have been developed and implemented, such as using k-means cluster analysis and random forest predictions, to ensure adequate accuracy on the data post-processing of LiDAR data simultaneously collected at different distances from the leading wind turbine rotor, both before and after the construction of the wind turbine array under investigation. The comparative analysis of these two data sets is aimed at differentiating the flow spatial variability associated with the site topography from the effects induced by the wind turbine rotors.

For this experiment, vertical profiles of horizontal wind speed, wind direction, and velocity dispersion were collected with four profiling wind LiDARs (*PLs* hereinafter) distributed over the site under investigation, both before and after the construction of an onshore array composed of four wind turbines. In particular, one profiling LiDAR (hereinafter named *PL*04) was located 10D upstream of the turbine array along the prevailing wind direction (West-South-West), thus it will be used to retrieve reference velocity profiles for the free-stream unperturbed condition. Nonetheless, previous works showed that wind speed could be affected by wind farm blockage even at such an upstream distance under stable atmospheric conditions.[12] The pre-construction data are first analyzed statistically and through the k-means cluster and random forest algorithms to

characterize the site climatology. Subsequently, the profiles of the velocity difference between the various profiling wind LiDARs and *PL*04 are investigated. Finally, the variability of the velocity difference measured before and after the construction of the turbine array will enable the differentiation of the spatial flow variability due to the site topography from the rotor-induced effects on the incoming ABL due to the wind turbine array.

The remainder of the paper is organized as follows. The site and experimental setup are described in Section 2, while the climatology survey of the site under investigation is provided in Section 3. The quantification of the rotor-induced effects through the profiling LiDAR measurements is reported in Section 4, then concluding remarks are provided in Section 5.

2 | SITE AND LiDAR FIELD CAMPAIGN

To investigate flow distortions on the incoming ABL due to the thrust force induced by wind turbine rotors, four Windcube V2 profiling wind LiDARs were deployed at an onshore wind farm located over relatively flat terrain in the northwest of the United States. The wind turbines under investigation have a rotor diameter, *D*, of 127 m, a hub height, *H*, of 89 m, and a rated power of 2.5 MW. Supervisory control and data acquisition (SCADA) data are provided as 10-min average and standard deviation of the hub-height wind speed, temperature, active power, thrust, generator RPM, and generator RPM set point. The positions of the four wind turbines considered in this work (*T*06–*T*09) and the locations of the profiling LiDARs (*PL*01-*PL*04) are reported in Figure 1A, while in Figure 1B, the wind rose measured at hub height with the profiling LiDAR *PL*04 shows the predominance of West-South-West wind directions, indicating that the profiling wind LiDARs are typically located upstream of the turbine array for the prevailing wind direction.

The four Windcube V2 profiling wind LiDARs were deployed to perform Doppler beam swinging (DBS) scans using a scanning cone half-angle of 28° from the vertical to generate 10-min-averaged profiles of the wind speed, direction, and velocity dispersion at the heights of 40 m, 64, m, 89 m (hub height), 114 m, 153 m, 160 m, 180 m, and 200 m. The dispersion parameter is an output of the LiDAR measurements quantifying the variability of the radial wind speed within each range gate. Therefore, under isotropic and homogeneous flow conditions, it can be considered a surrogate parameter for wind turbulence intensity. The LiDAR *PL*04 is devoted to characterizing the nearly unperturbed wind conditions having a distance of about 10*D* for the prevailing wind direction, while the other LiDARs might be affected more significantly by the rotor-induced flow modifications. Measurements were performed both before (from June 18, 2020, until August 11, 2020) and after (from December 15, 2020, to June 14, 2021) the construction of the wind farm, hereafter named "Phase 1" and "Phase 3," respectively. Between these two phases of the project, namely, during "Phase 2," all the profiling wind LiDARs were co-located to assess their calibrations and measurement accuracy. The linear regression analysis performed for the radial velocity data collected with all the profiling LiDARs co-located and measuring with the same settings at the same height, not shown here for the sake of brevity, returned an average percentage error smaller than 0.2%, a correlation coefficient always larger than 0.998, and intercept smaller than 0.2 m/s.[6]

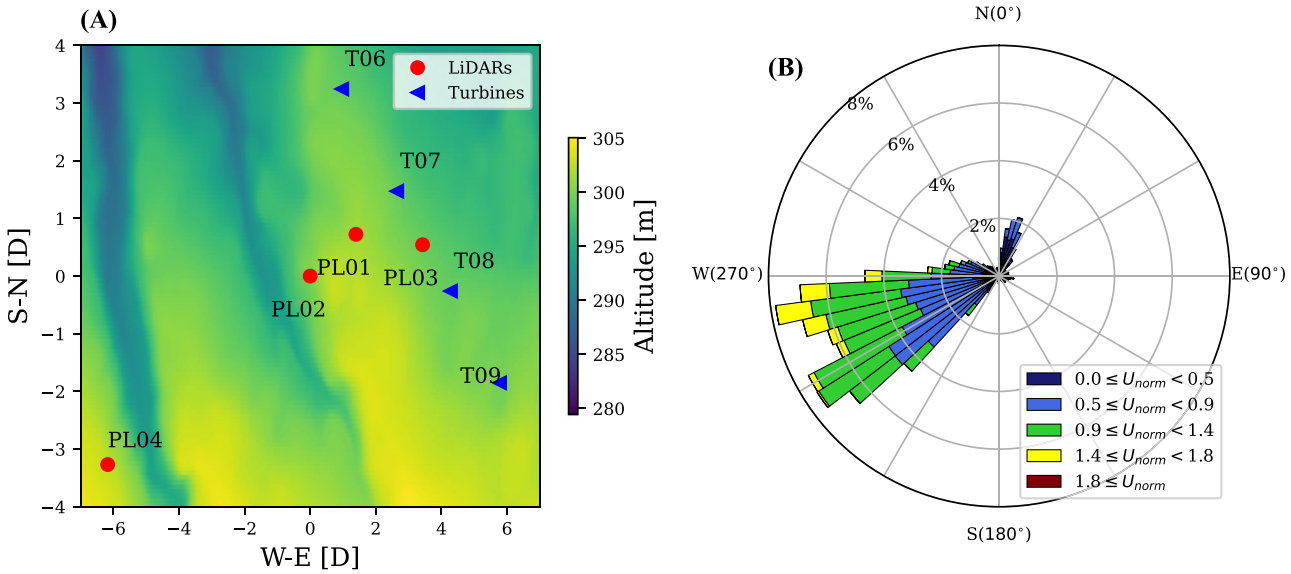

FIGURE 1 Experimental site: (A) Layout of the wind turbines and profiling wind LiDARs; (B) wind rose retrieved from the hub-height measurements collected from the *PL*04 profiling wind LiDAR normalized by the turbine rated wind speed of 10 m/s.

3 | SITE CLIMATOLOGY

To investigate the climatology of the site through a k-means cluster analysis[25] and random-forest predictions,[26,27] we consider data collected from the profiling LiDAR *PL*04 both during the pre-construction phase (Phase 1) and the post-construction phase (Phase 3) of the project. The initial data set comprises 8065 and 26,209 data samples for Phases 1 and 3, respectively, which are then reduced to 6826 and 13,260 after removing time stamps when not all the data were simultaneously available, for a total of 20,086 samples available for the climatology study.

The statistics of the velocity profiles from *PL*04 are reported in a dimensional form in Figure 2A, and in Figure 2B made non-dimensional with the horizontal velocity measured at 200-m height, which is referred to as U_∞, and assumed as the unperturbed free-stream velocity being above rotor heights and at a distance of about 10*D* from the turbines under investigation. The variability around the mean of the *PL*04 velocity profiles

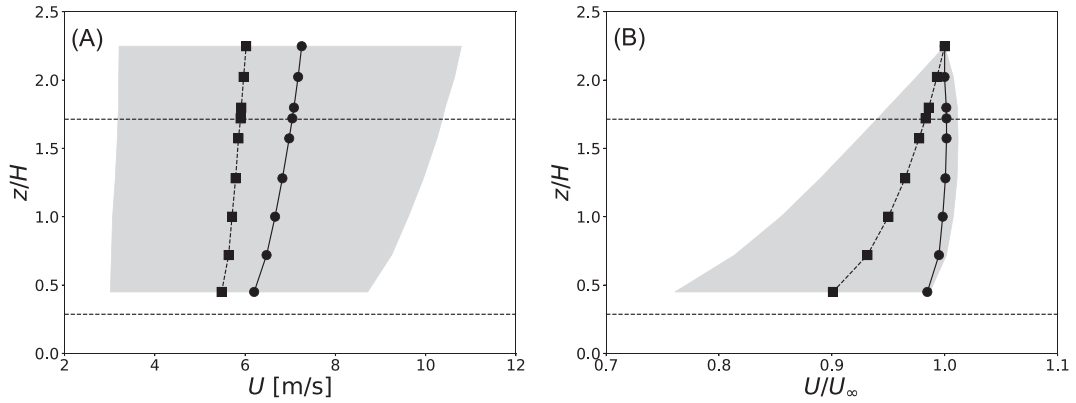

FIGURE 2 Statistics of the velocity profiles from the profiling LiDAR *PL*04: (A) dimensional form; (B) non-dimensional form with U_∞ measured from *PL*04 at 200-m-height. The grey zone represents the 25–75 percentile range, while the square and circle markers report median and mean values, respectively. The dashed lines indicate the bottom and top tips of the wind turbine rotor.

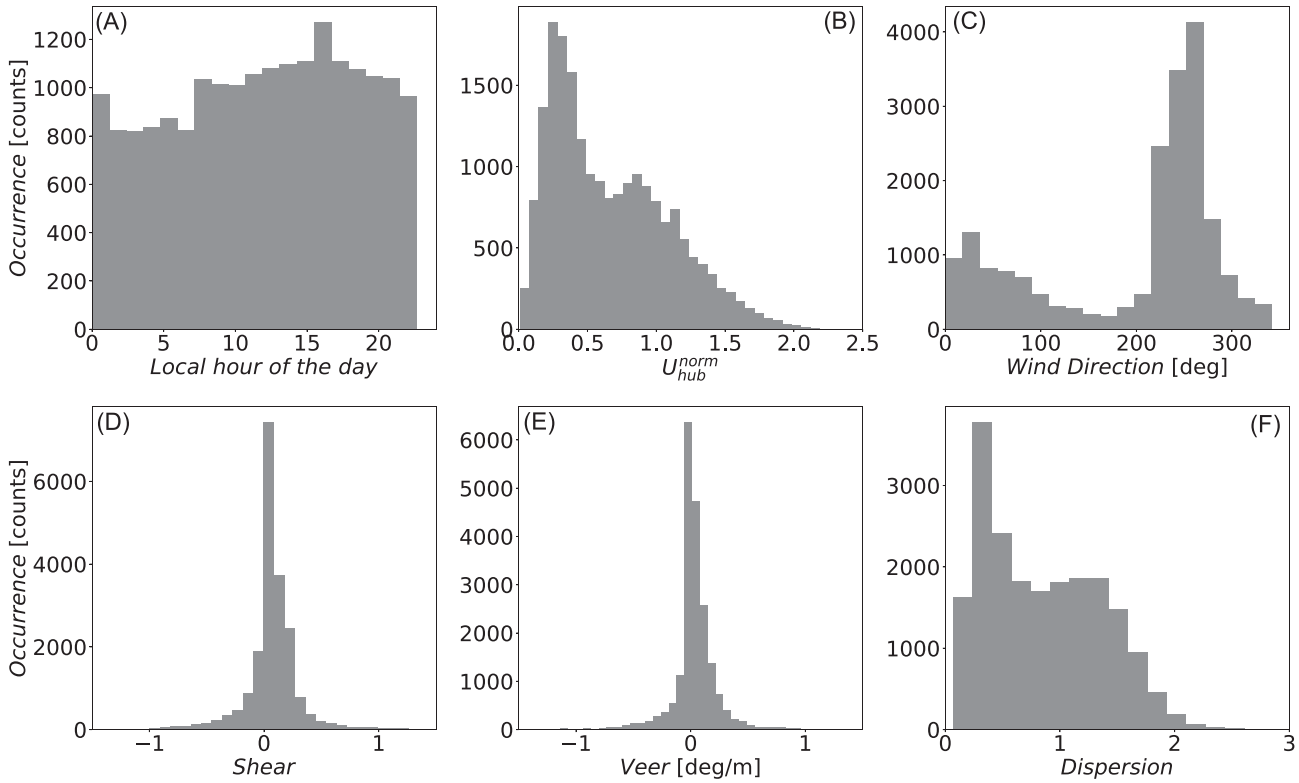

FIGURE 3 Histograms of the parameters obtained from the profiling LiDAR *PL*04 data: (A) Local time of the day; (B) hub-height wind speed normalized by the turbine rated wind speed; (C) wind direction at hub height; (D) shear; (E) veer; (F) velocity dispersion.

(quantified in Figure 2 by the gray region, encompassing the 25th to 75th percentile area) shows wide ranges of wind speed, and shear for the wind field occurring over this site, thus deserving a more in-depth analysis.

The velocity profiles collected from *PL*04 are classified through the local time of the day, hub-height wind speed, wind direction, shear, veer, and LiDAR velocity dispersion. The shear is quantified here through the fitting of the shear exponent, α, on each velocity profile[28–30]:

$$\alpha = \frac{\log\left(U/U_R\right)}{\log\left(z/z_R\right)}, \tag{1}$$

where U and z are horizontal wind speed and height, respectively, while the subscript "R" refers to reference values, which are assumed at the lowest available height. For the dataset under investigation, fitting of velocity profiles showing a canonical trend with positive shear can produce mean R^2 values as high as 0.91, while velocity profiles exhibiting a low level jet or negative shear have smaller R^2 values (minimum value 0.58). Veer is quantified as the slope of the linear variation of wind direction with height calculated from each vertical profile of the wind direction. The histograms of the above-mentioned parameters are reported in Figure 3.

This preliminary climatology analysis indicates some site-specific features, such as the occurrence of two peaks in the histogram of the hub-height wind speed in Figure 3B. Specifically, the hub-height wind speed normalized by the rated wind speed of the wind turbines (10 m/s), U_{hub}^{norm}, with the highest occurrence is around 0.3, while a second peak is detected at around 0.9. The histogram of the wind direction (Figure 3C) confirms the prevalence of westerly winds for this site, which is a favorable wind sector to investigate blockage according to the layout of the LiDAR wind profilers depicted in Figure 1. Interestingly, the histograms for shear and veer in Figure 3D and 3E, respectively, show roughly symmetric probability of occurrence of positive and negative events. Finally, in Figure 3F, the LiDAR velocity dispersion shows a peak around 0.3 and a gradually decreasing occurrence for values larger than 1.5.

More details on the site climatology are obtained from the two-dimensional histograms for coupled parameters reported in Figure 4. From Figure 4A, it is noticed that events with large positive shear ($\alpha > 0.02$) generally occur for U_{hub}^{norm} larger than 0.5, while for $U_{hub}^{norm} < 0.5$ there is a roughly equal probability to observe ABL flows with either positive and negative shear. A similar feature is observed for veer in Figure 4B, namely, conditions with both positive and negative veer can occur for $U_{hub}^{norm} < 0.5$, while veer is generally non-negative for higher wind speeds.

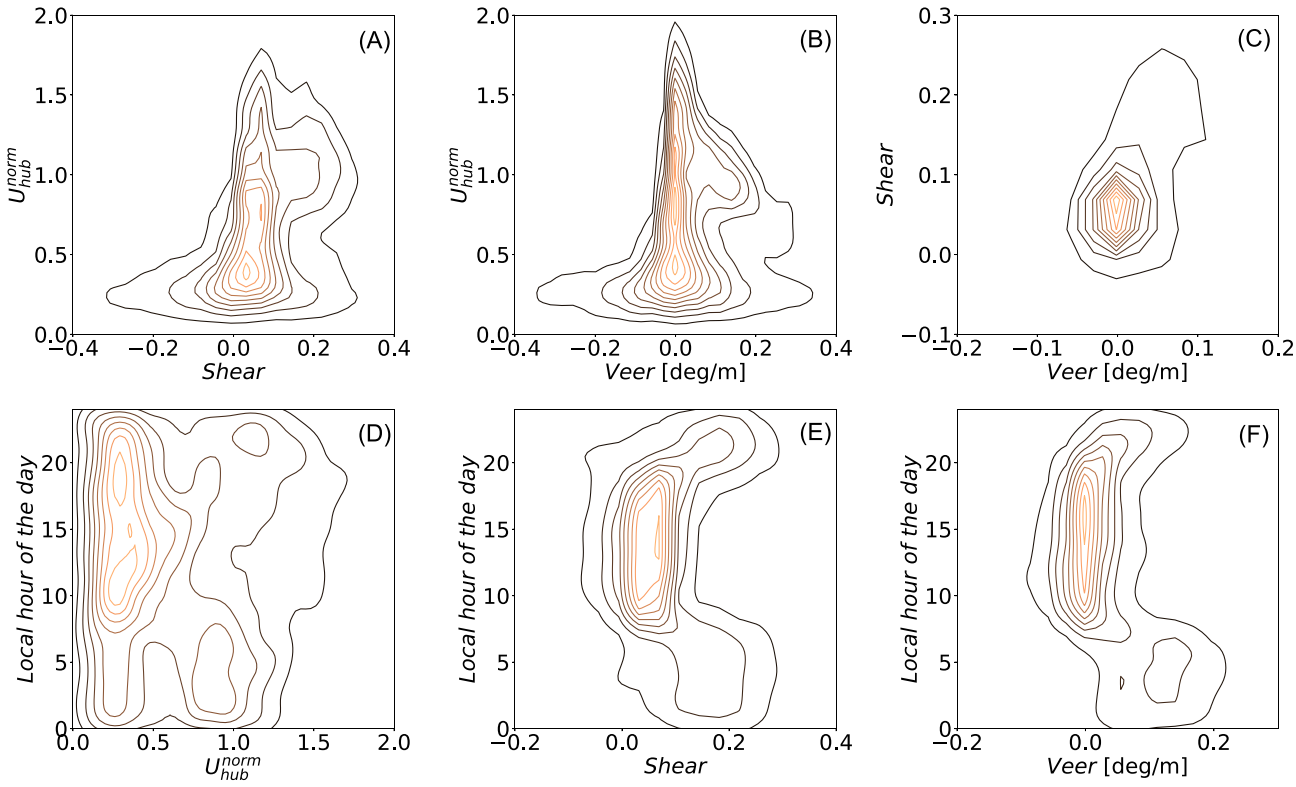

FIGURE 4 2D histograms of the parameters from the velocity profiles of *PL*04: normalized hub-height wind speed versus (A) shear, (B) veer, and (D) local time of the day; shear versus (C) veer, and (E) local time of the day; (F) local time of the day versus veer. The histograms have 10 evenly-spaced levels of the iso-contours (brighter colors for higher occurrence counts).

Figure 4E and 4F show that events with significant shear ($\alpha > 0.1$) and veer (>0.1 deg/m), respectively, typically occur at nighttime, which might be associated with stable atmospheric conditions. Nonetheless, Figure 4C suggests that the correlation between shear and veer is roughly negligible (correlation coefficient equal to −0.08), which indicates that high-shear conditions can occur with negligible veer and vice versa.

The characterization of the typical wind profiles occurring over this site is performed through the cluster analysis of the normalized velocity profiles collected from the profiling LiDAR *PL*04 during Phases 1 and 3 of the experiment. This task is performed through the k-means algorithm

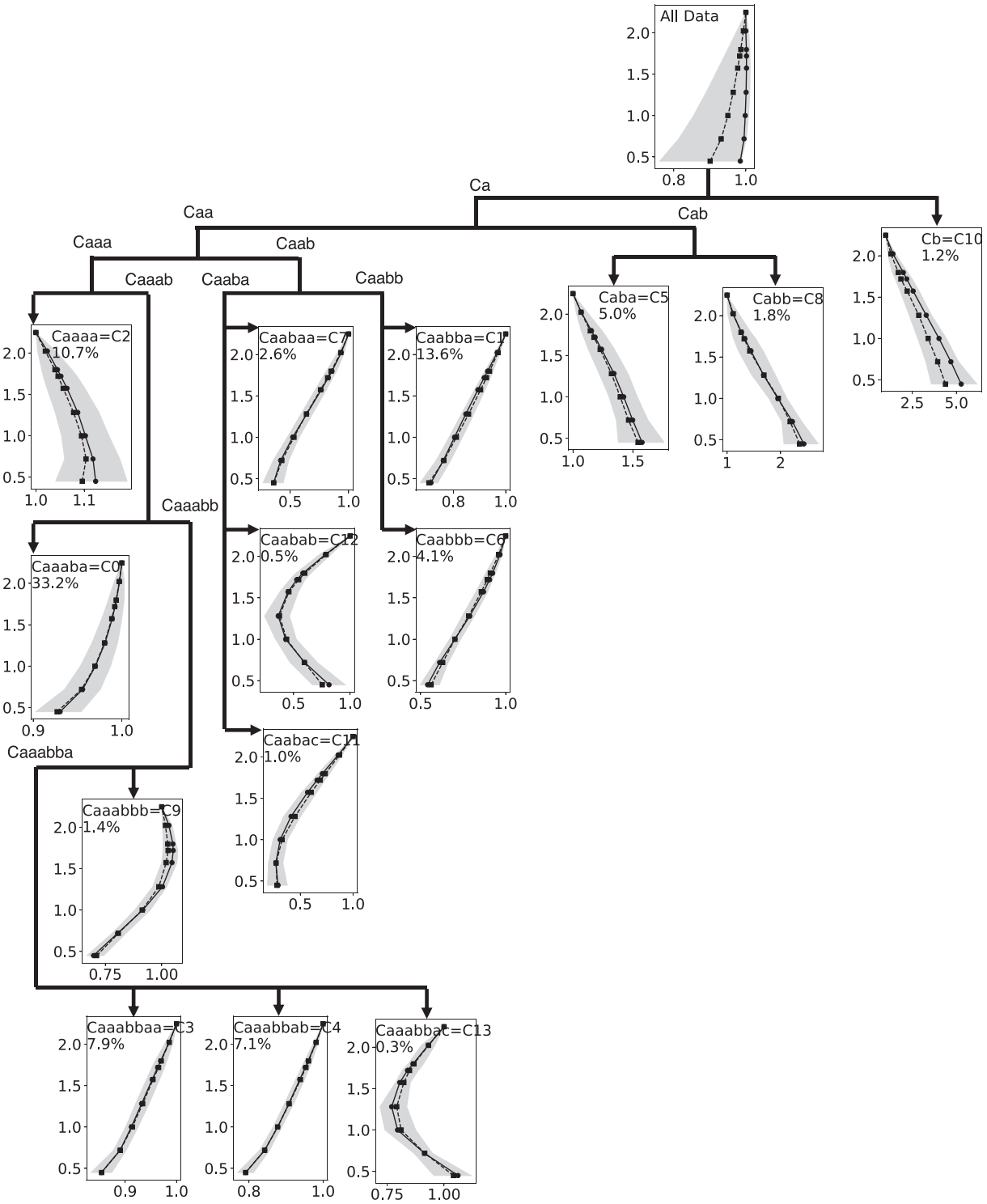

FIGURE 5 Dendrogram of the velocity profiles from the profiling LiDAR *PL*04. For each cluster, data are reported similarly to Figure 2B where the parameter on the *x*-axis is the normalized wind speed, U/U_∞, and on the *y*-axis the normalized height, z/H, while the dendrogram label, the final cluster label, and the percentage occurrence are reported as well.

with the dendrogram approach,[23,31] for which clusters are generated based on their inertia value; the latter is an output of the k-means algorithm indicating the statistical significance of each cluster. Once the clusters are generated, each cluster is considered a "node" of the dendrogram, and it is further partitioned into sub-clusters to generate a cluster analysis following a tree-like structure, namely, the dendrogram.

For each cluster, a silhouette analysis is performed to reject samples that might be ascribed to a specific cluster without high statistical significance.[32] The silhouette coefficient can assume values between −1 and 1, and non-positive values indicate samples that might belong to the interface among adjacent clusters and, thus, are rejected for further analyses. For the data set under investigation, 90.4% of the initial dataset is retained.

Following the dendrogram approach, 14 clusters are generated from the normalized profiles of *PL*04, which are shown in the dendrogram of Figure 5 by reporting mean and median profiles within each cluster of the normalized velocity, U/U_∞, the 25th–75th percentile region with a grey area, the initial label assigned to the clusters based on the dendrogram, for example, *Cabcd*, the final label of the cluster from *C*0 up to *C*13, and the percentage occurrence. These velocity statistics are reported versus height normalized by the wind-turbine hub height, *H*. This climatology survey performed through a cluster analysis allows highlighting the occurrence of a broad variety of velocity profiles with different levels of wind shear, both positive and negative. It is noteworthy that mean velocity profiles for some clusters can be adequately modeled with the power law of Equation (1) (e.g., C1, C3, C4, C6, and C7). In contrast, other velocity profiles, such as for C2, C11-C13, the value of the shear exponent can only provide bulk information on wind shear even though fitting with the power law is relatively poor.

The generated clusters are subsequently sorted based on their percentage occurrence, as reported in Figure 6 with their final label. For Figures 6,7, and 8, statistics for each cluster are reported with the same color to facilitate the interpretation of the data analysis presented. The representativeness of the cluster center, that is, the mean velocity profile within each cluster, is quantified through the mean absolute percentage error (MAPE), which is reported in Table 1 for the various clusters together with other statistical parameters. The first five clusters have a MAPE smaller than 6% while the median MAPE across all the clusters is 5.95%, which indicates a good level of classification and predictability of the data set through the k-means cluster analysis.

The first five clusters, *C*0–*C*4, encompass a total occurrence of about 72% of the entire dataset (see Table 1). The first two clusters with the largest occurrence, that is, *C*0 and *C*1, are typical boundary layer velocity profiles with positive shear (median shear equal to 0.05 and 0.20, respectively), while *C*2, which has a percentage occurrence of 10.7%, has a negative median shear of −0.04, which is not a canonical wind condition for the ABL. The occurrence of velocity profiles with negative shear (total occurrence of about 20% of the selected data set), which is not

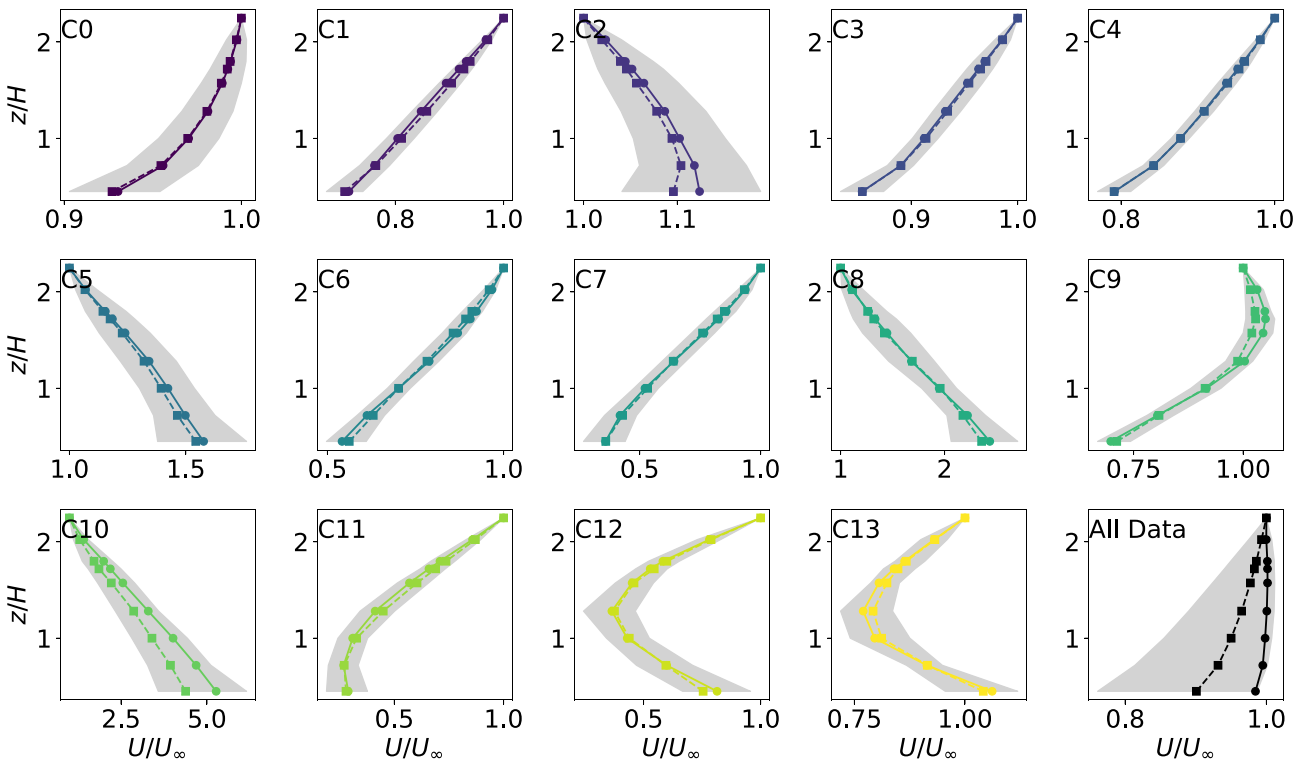

FIGURE 6 Statistics of the velocity profiles from *PL*04 for the various clusters. The representation is similar to Figure 2B. The limits on the horizontal axis are different for the various panels.

TABLE 1 Cluster parameters.

Cluster Number	Label	Occurrence [%]	U_{hub}^{norm}	Shear	Veer [°/m]	Dispersion	MAPE [%]
C0	Caaaba	33.2	0.77	0.05	0.002	1.20	2.0
C1	Caabba	13.6	0.91	0.20	0.063	0.77	3.4
C2	Caaaa	10.7	0.35	−0.04	0.047	0.49	5.5
C3	Caaabbaa	7.9	0.71	0.09	0.017	1.00	1.5
C4	Caaabbab	7.1	0.97	0.14	0.045	0.84	1.5
C5	Caba	5.0	0.30	−0.21	0.091	0.32	10.2
C6	Caabbb	4.1	0.36	0.35	0.046	0.42	5.7
C7	Caabaa	2.6	0.23	0.60	−0.056	0.37	8.1
C8	Cabb	1.8	0.28	−0.44	0.093	0.33	14.5
C9	Caaabbb	1.4	0.48	0.26	0.0053	0.42	4.4
C10	Cb	1.2	0.25	−0.70	0.042	0.32	32.6
C11	Caabac	1.0	0.13	0.61	−0.210	0.39	13.1
C12	Caabab	0.5	0.11	−0.19	−0.190	0.27	16.1
C13	Caaabbac	0.3	0.22	−0.13	0.190	0.29	6.2

Note: Wind parameters are reported as median values calculated within each cluster.

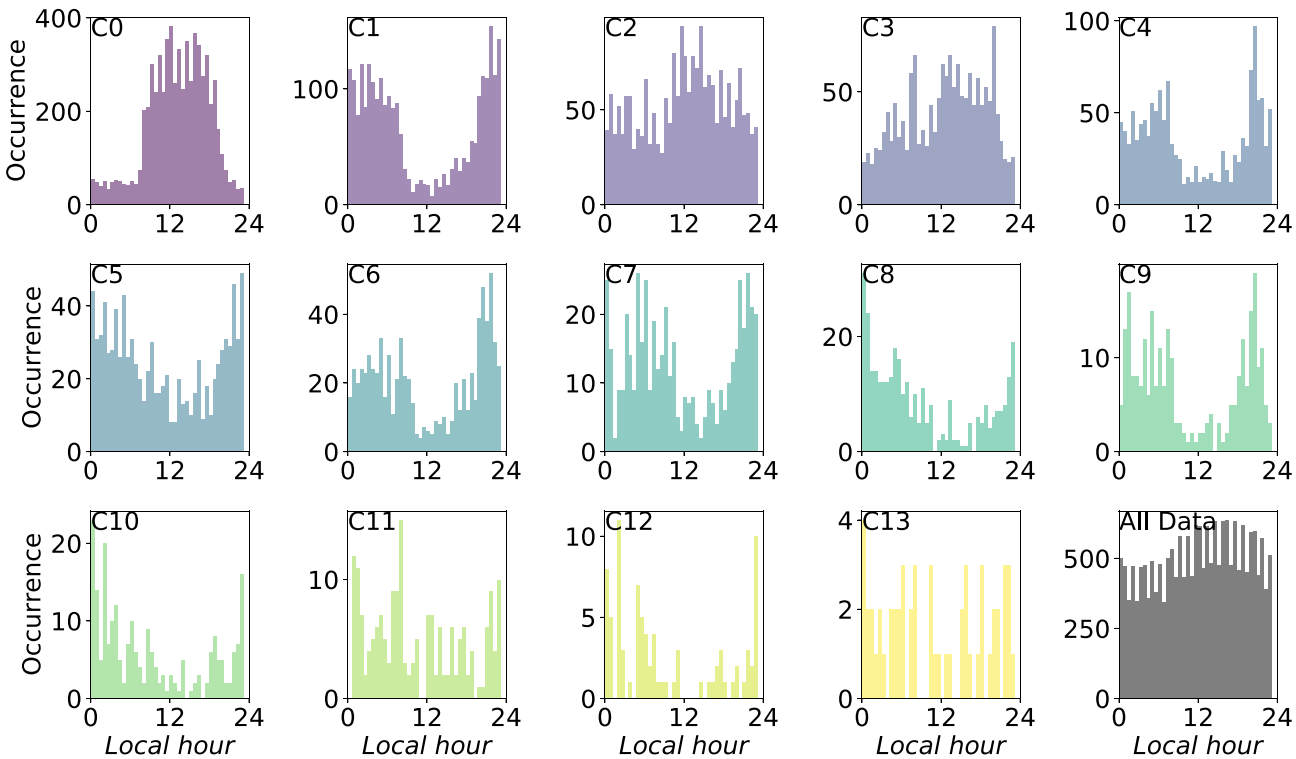

FIGURE 7 Histograms of the local time for the various clusters of the *PL*04 data.

only associated with cluster *C*2 but also with other clusters (such as *C*8 and *C*10), corresponds typically to relatively low wind speeds of the incoming wind field, that is, with $U_{hub}^{norm} \lesssim 0.4$.

Other clusters with different levels of positive and negative shear are identified as well. It is noteworthy that *C*9 is associated with a low-level jet condition occurring with its nose just above the top tip of the turbines with an occurrence of 1.4% over the entire data set. The last two clusters (*C*12 and *C*13), with a total occurrence of 0.8%, represent peculiar wind conditions with shear switching from negative to positive with increasing height across the rotor area. These wind conditions, even if infrequently, occur with very low hub height wind speed (median

U_{hub}^{norm} of 0.11 and 0.22, respectively), and with significant veer yet with opposite signs (median veer of −0.19 and 0.19 for *C*12 and *C*13, respectively).

We can now investigate the effects of the cluster analysis on other parameters for the wind profiles measured by the LiDAR *PL*04, namely, the time of the day, hub-height wind speed, and shear, which were not provided directly as inputs of the k-means algorithm. For instance, in Figure 7, the histograms of the time of the day for the various clusters show that clusters *C*0, *C*2, and *C*3 are mainly associated with daytime operations, while the remaining ones, except *C*13, show a majority of occurrences during nighttime. This result indicates that the daily cycle of atmospheric stability can significantly drive the variability in wind conditions, especially in terms of wind shear. Furthermore, the typical daytime conditions represented by the cluster centers of *C*0, *C*2, and *C*3 show a better level of predictability than nighttime wind conditions. Indeed, with only three clusters a total occurrence of about 52% is captured, while a larger number of clusters is needed to represent the typical wind conditions measured at nighttime. This analysis is corroborated by the median MAPE of the velocity profiles with respect to their cluster center reported in the last column of Table 1. The clusters *C*0, *C*2, and *C*3 all have median MAPE below 6%, while larger values are estimated for most of the remaining clusters.

The histograms of the hub-height wind speed normalized by the turbine rated wind speed, U_{hub}^{norm}, calculated for the various clusters are reported in Figure 8. It is noteworthy that the only clusters that occur for a wide range of wind speeds, namely, both below and above the wind turbine rated wind speed, are clusters *C*0, *C*1, *C*3, *C*4, and *C*9, for a total occurrence of about 63% of the entire data set. This means that the main variability, and thus lower likelihood to make predictions with good accuracy, in the incoming velocity profiles is mainly associated with relatively low wind speeds. The clusters with higher hub-height wind speed have typically positive wind shear; however, cluster *C*9 is associated with the presence of low-level jets.

We now investigate the capability of predicting the velocity profiles measured by the LiDAR *PL*04 by providing as inputs the background flow parameters, such as time of the day, hub-height wind speed, wind direction, shear, veer, and velocity dispersion. These predictions are performed with the random forest algorithm available from the Scikit-learn package in Python.[33] The input data set is split into 90% portion for training and 10% for testing. For the random forest, a maximum depth of 50 and a learning rate of 0.3 are selected upon a preliminary sensitivity study on the accuracy of the random forest predictions (weakly affected though by the model parameters). The output generated from the random forest is the most probable cluster associated with the provided inputs. The accuracy of the random forest predictions is then assessed through the percentage of true predictions on the cluster number associated with each velocity profile within each cluster and for the entire data set. The results of the random forest predictions of the *PL*04 velocity profiles are summarized in Table 2 for the various models tested.

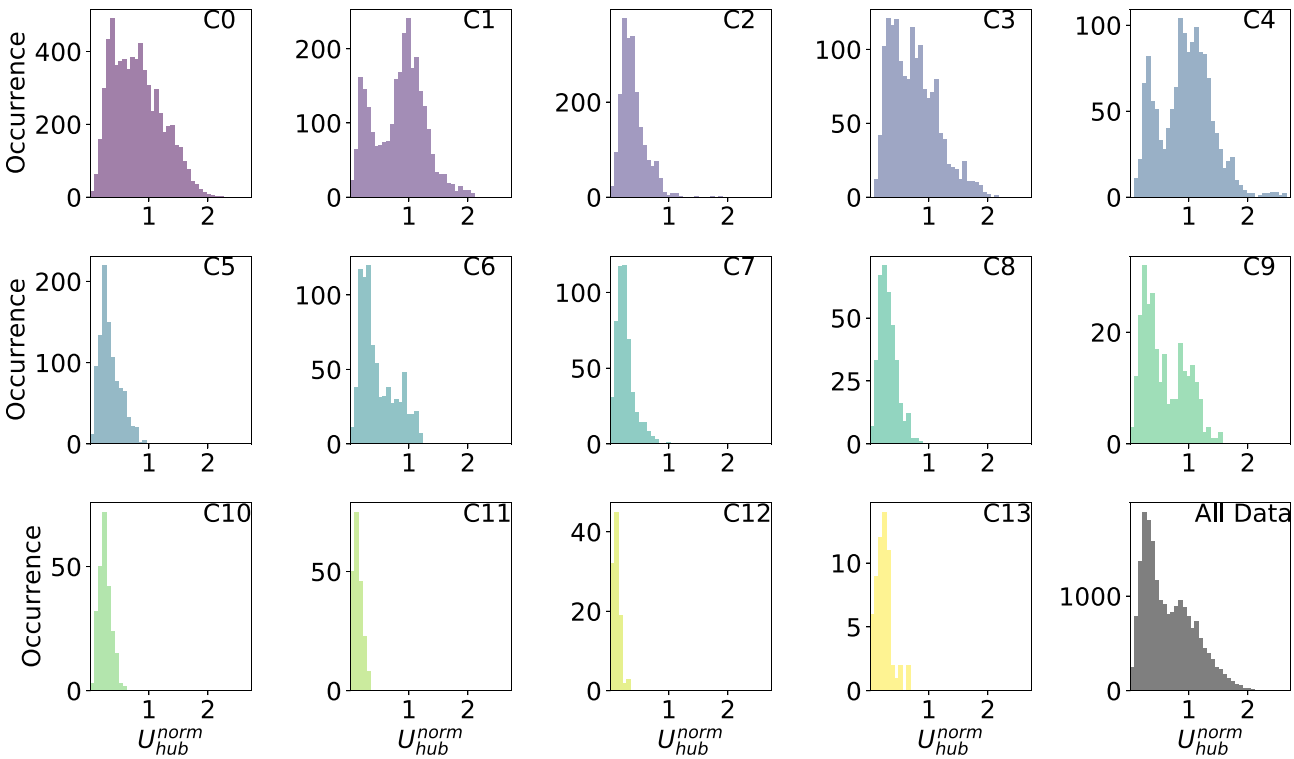

FIGURE 8 Histograms of the normalized hub-height wind speed for the various clusters of the *PL*04 data.

TABLE 2 Percentage of true predictions for the velocity profiles of the LiDAR *PL*04 through random forest.

Inputs	C0	C1	C2	C3	C4	C5	C6	C7	C8	C9	C10	C11	C12	C13	Total
Time	85	58	0	0	0	0	0	0	0	0	0	0	0	0	44.2
U_{hub}	96	2	11	1	2	8	2	6	0	0	4	11	23	0	43.6
Wind Dir.	89	34	10	3	8	11	2	5	4	0	2	1	0	0	45.5
Shear	76	73	54	23	52	63	38	65	18	3	70	0	0	0	61.4
Veer	87	37	19	3	4	18	4	15	5	1	7	22	40	2	46.8
Dispersion	96	10	3	0	0	3	0	1	0	0	0	4	0	0	43.1
Time, U_{hub}	85	58	26	7	18	34	15	24	15	6	17	28	50	0	52.7
Time, Wind Dir.	86	61	18	11	20	22	30	27	14	14	14	8	7	0	53.1
Time, Shear	79	75	54	27	52	61	47	67	29	4	64	8	5	0	63.6
Time, Veer	84	61	28	10	20	24	16	22	14	5	15	27	43	2	53.0
Time, Dispersion	88	60	19	6	16	19	13	7	9	2	5	9	7	2	51.8
U_{hub}, Wind Dir.	86	48	44	20	29	42	29	34	20	4	23	28	43	3	57.1
U_{hub}, Shear	79	78	57	32	45	64	51	74	24	5	67	29	33	5	65.1
U_{hub}, Veer	85	57	35	10	18	31	16	25	19	4	21	38	55	2	54.1
U_{hub}, Dispersion	84	44	26	10	14	32	16	20	16	4	9	22	25	2	50.0
Wind Dir., Shear	78	75	57	33	56	60	45	68	43	10	64	8	5	2	64.9
Wind Dir., Veer	90	74	61	38	45	58	49	47	39	27	43	44	55	7	69.8
Wind Dir., Dispersion	84	48	23	9	17	26	23	21	18	9	15	9	5	2	50.4
Shear, Veer	79	79	56	32	47	65	48	73	31	7	58	47	50	5	65.4
Shear, Dispersion	79	73	54	28	46	62	47	61	31	14	67	4	3	0	63.4
Veer, Dispersion	85	51	28	6	11	32	16	22	12	5	12	31	50	0	51.4
U_{hub}, Wind Direction, Shear	86	84	70	54	67	71	69	79	58	34	75	60	58	20	76.6
U_{hub}, Wind Direction, Veer	92	82	75	54	61	73	68	68	59	48	59	66	71	27	78.9
Time, Wind Direction, Shear	92	90	83	74	81	83	82	84	79	70	88	63	50	36	86.3
Time, Wind Direction, Veer	93	87	79	72	76	76	78	75	68	72	70	69	77	46	84.6
U_{hub}, Wind Direction, Shear, Veer	93	93	85	79	85	86	85	87	79	73	88	83	81	51	88.7
Time, Wind Direction, Shear, Veer	93	92	83	74	82	84	83	84	76	67	86	78	75	44	87.0
Time, U_{hub}, Shear, Veer	93	92	83	74	82	84	83	84	76	67	86	78	75	44	89.4
Time, U_{hub}, W.D., Shear, Veer	93	94	87	82	86	88	88	89	81	78	91	83	87	64	90.0
Time, U_{hub}, W.D., Shear, Veer, Disp.	94	93	87	82	87	88	90	90	83	78	89	82	89	66	90.3

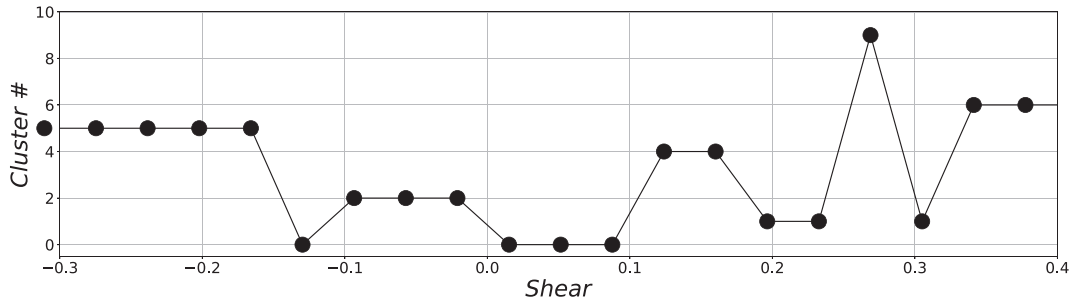

FIGURE 9 Cluster prediction with random forest by using as input wind shear.

The predictions obtained with random forest by providing a single input parameter do not seem highly satisfactory. Nonetheless, the highest percentage of true predictions is achieved when using wind shear as the input parameter, namely, 61.4% of true predictions, while a few clusters are predicted with an accuracy larger than 70%. The clusters predicted by varying wind shear between the 5th and 95th percentile of the values measured by the LiDAR *PL*04 during the field campaign are reported in Figure 9. For wind shear lower than −0.2, the predicted velocity profile is

that associated with *C*5 (see Figure 6), which is indeed characterized by a low median shear of −0.21. This is not the mean velocity profile with the lowest wind shear, yet the only one with an occurrence larger than 2%, which makes it the most probable. For slightly negative wind shear, the velocity profile of *C*2 is predicted (occurrence of 10.7%), which has a median shear of −0.04. Switching to conditions with positive shear, the clusters *C*0, *C*4, *C*1, and *C*9 are predicted with increasing shear. Finally, the velocity profile predicted for the largest shear values is *C*6, which has a median shear of 0.35.

To increase accuracy in the predictions of the freestream velocity profiles with random forest, we provide two input parameters. Indeed, the true prediction percentage increases from 43% to 61% (median 44.8%) for single-input models to 50% to 70% range (median 54.1%) for two-input models (cf., with Table 2). The highest accuracy for the two-input models is achieved using wind direction and veer (69.8%), followed by the model using wind shear and veer (65.4%). By increasing the model inputs to three, we achieve the most significant improvement in the percentage of true predictions (between 77% and 86%). The highest accuracy is achieved by using time of the day, wind direction, and shear. By gradually increasing the number of inputs, the model accuracy keeps increasing, up to a maximum of 90.3% when all six wind parameters are used.

In summary, we have been able to characterize with good accuracy the climatology of the site under investigation through cluster analysis. A total of 14 clusters is deemed to be sufficient to reproduce the variability of the ABL velocity profiles, including conditions with various positive shear, negative shear, low-level jets, and even flows with negative shear close to the ground and positive shear aloft. The representation of the ABL profiles through the cluster mean profiles leads to a median MAPE below 6% within each cluster, which indicates that using the velocity profiles associated with the various cluster centers is a good strategy for developing a potential surrogate model to predict the incoming wind field from a few freestream parameters. Indeed, it has been shown that accurate predictions of the most probable freestream mean velocity profile can be achieved with random forest by providing as input various background flow parameters. Specifically, only providing incoming wind shear, a very good prediction accuracy of 61.4% is already achieved. Overall, the results show a high level of repeatability and predictability of the incoming wind velocity profile for different wind conditions.

4 | BLOCKAGE ANALYSIS FROM PROFILING WIND LiDAR DATA

The strategy used in this work to investigate rotor-induced effects on the incoming wind field consists in analyzing the instantaneous difference between the velocity profile measured by the LiDAR *PL*04, which is located at an upstream distance of about 10*D* for the prevailing wind sector ($217^\circ \le \theta_w \le 247^\circ$), and the other profiling LiDARs, which are located in the proximity of the wind turbines and, thus, can be affected by the pressure field induced by the turbine rotors. The variation of the velocity difference among different LiDARs and LiDAR *PL*04 measured before (Phase 1) and after (Phase 3) the construction of the turbine array should enable the differentiation of the wind variability associated with site climatology and terrain characteristics from that induced by the wind turbine rotors. Nonetheless, it is worth remembering that considering the small number of wind turbines comprised in the wind farm under investigation, it is difficult to differentiate between the velocity modifications associated with single-turbine induction and cumulative blockage effects of the wind farm.

Based on the climatology study presented in Section 3, wind conditions with normalized hub-height wind speed lower than 0.5 (recorded from the SCADA at the turbines *T*07 or *T*08) are disregarded for this analysis to avoid non-canonical conditions with large shear or with either positive or negative veer values (see Figure 4). Further, selected operating conditions of the wind turbines *T*07 and *T*08, which have active pitch control, are disregarded because of the smaller thrust coefficients for the turbine rotors (e.g., see previous works[23,24,34]) and, thus, smaller blockage effects on the incoming wind field.[3,10,12] This criterion is implemented by rejecting wind turbine operations of turbines *T*07 and *T*08 with a normalized hub-height wind speed recorded by the SCADA larger than 0.8.

During Phase 3 of the project, the wind turbines were often de-rated due to grid constraints; these operative conditions are disregarded as well. Finally, quality control of the SCADA and LiDAR data is also performed by selecting only time stamps when SCADA, LiDAR *PL*04, and the other selected LiDAR under investigation are simultaneously available and quality controlled. For instance, for the simultaneous analysis of the LiDARs *PL*04 and *PL*01, from an initial availability of 8065 and 26,209 samples for Phase 1 and 3, respectively, we down-selected 2544 and 4732 samples, respectively, for the wind sector $217^\circ \ge \theta_w \ge 247^\circ$ investigated for wind farm blockage, then down to 1861 and 202 for Phase 1 and Phase 3, respectively, by applying the above-mentioned filters and the quality control process. The large reduction in data availability for the Phase-3 data set is mainly associated with the de-rating of the wind turbines, as shown in Figure 10. Specifically, to down-select operative conditions with a roughly constant thrust coefficient, C_t, the normalized hub-height wind speed is constrained as $0.5 \le U_{hub}^{norm} \le 0.8$ and de-rated conditions disregarded, which correspond to the red points in Figure 10A for turbine *T*07. For the selected samples, also the power coefficient is approximately close to its maximum and with small variability, as shown in Figure 10B. Finally, the power and thrust of the initial and down-selected data set are reported in Figure 10C and 10D, respectively.

Histograms of the most representative parameters down-selected for both Phase 1 and Phase 3 are reported in Figure 11. Besides the much larger number of data available for Phase 1 than for Phase 3, both data sets show a large predominance of nighttime conditions, though wind shear does not have a clear offset. Indeed, the median values for wind shear are equal to 0.12 and 0.05 for Phase 1 and Phase 3, respectively. In

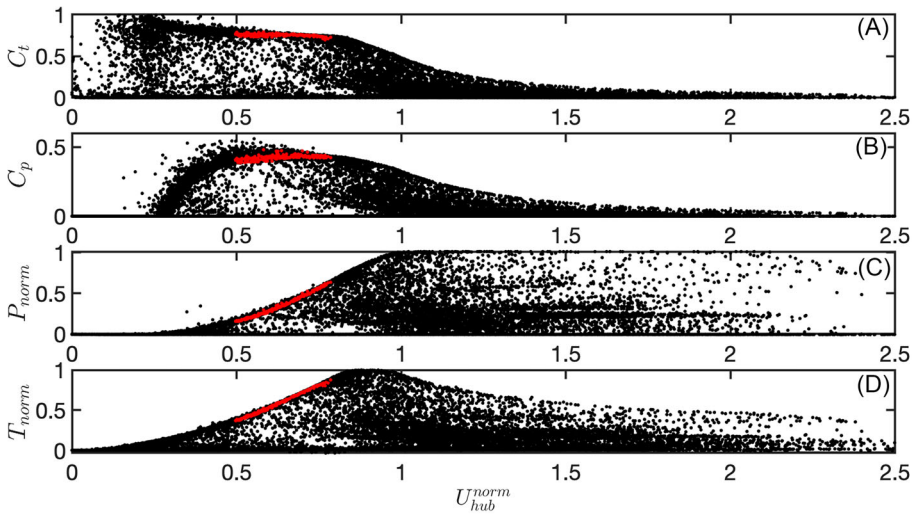

FIGURE 10 Raw (black) and down-selected (red) SCADA data for turbine *T*07: (A) Thrust coefficient; (B) power coefficient; (C) normalized power; (D) normalized thrust.

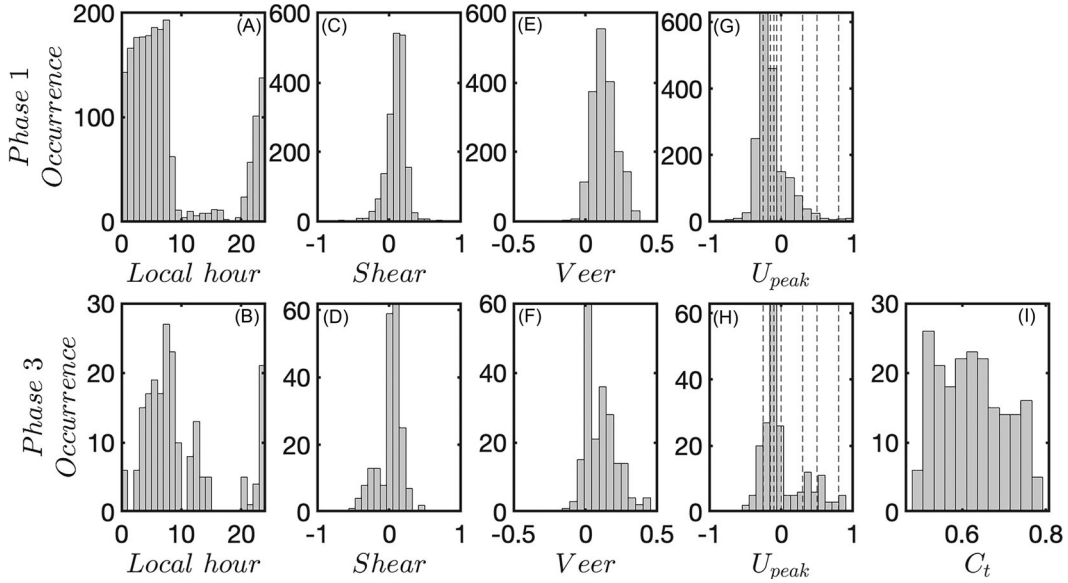

FIGURE 11 Histograms of the parameters for the data sets down-selected from Phase 1 (top row) and Phase 3 (bottom row) of the experiment from the profiling LiDAR *PL*04 and SCADA.

contrast, the majority of the down-selected wind profiles measured by the profiling LiDAR *PL*04 have positive veer (median values of 0.12 and 0.10 for Phase 1 and Phase 3, respectively).

To characterize the incoming ABL velocity profile, while avoiding potential misinterpretations by only using wind shear due to the occurrence of wind conditions showing both positive and negative shear at different heights or low-level jets (see, e.g., Figure 6), we define the following velocity parameter for the data measured from the profiling LiDAR *PL*04:

$$U_{peak} = \pm \max_{z_i} \{|U(z_i)/U_\infty - 1|\}, \tag{2}$$

where the sign $\pm$ associates $+$ $(-)$ in case the identified maximum corresponds to a positive (negative) value of $(U/U_\infty - 1)$. If $U_{peak} = 0$, then the velocity profile measured by *PL*04 has zero shear and the wind velocity is constant over the measured heights (within the limit of the accuracy considered). If $U_{peak} < 0$, then we can expect a velocity deficit with respect to the freestream condition aloft and, thus, a velocity profile with a general positive shear; the more negative is U_{peak}, the larger the wind shear. In contrast, if $U_{peak} > 0$ then, we can observe velocity excess with respect to the freestream condition aloft and, thus, a velocity profile with generally negative shear or a low-level jet.

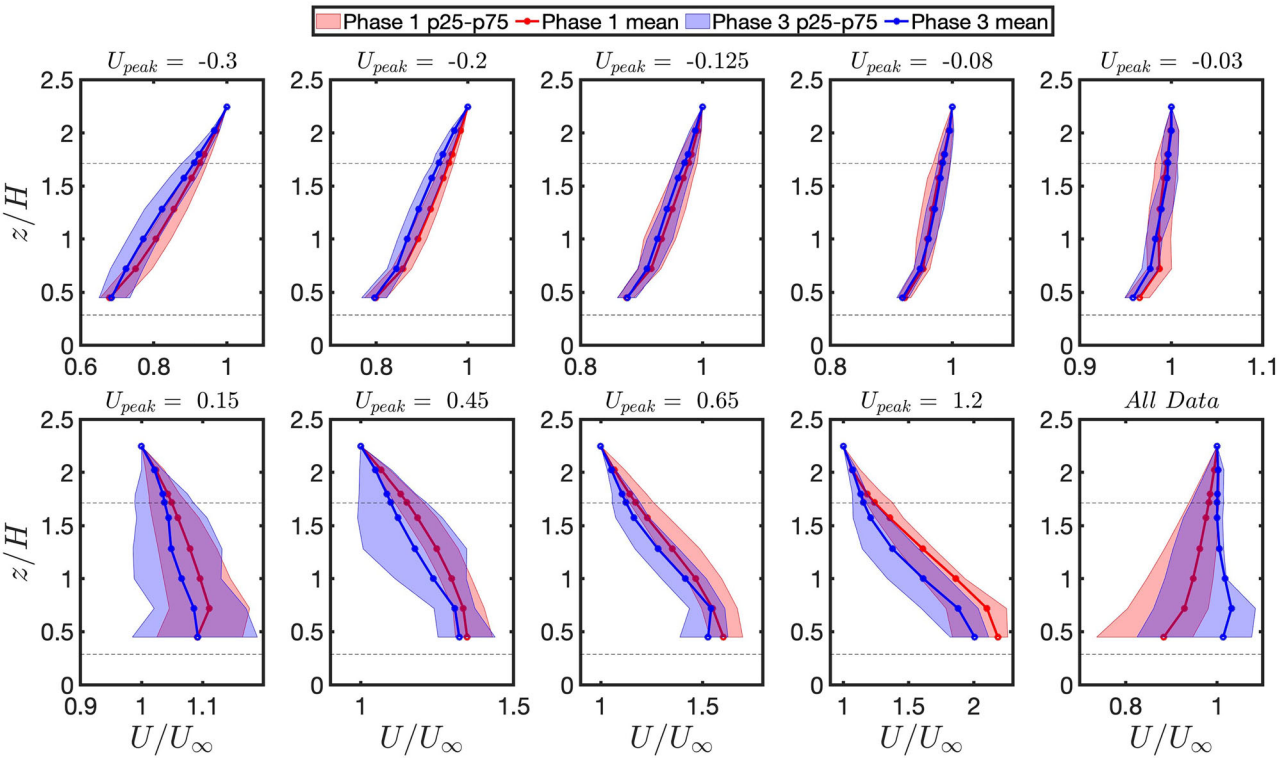

FIGURE 12 Binned statistics of the normalized velocity profiles measured by the LiDAR *PL*04. The bin centers are indicated as the title of each panel in terms of U_{peak}. The shaded areas represent the interval between the 25th and 75th percentile, while the lines are the mean values. Red and blue data correspond to Phase 1 and Phase 3, respectively. The horizontal dashed lines delimit the rotor heights. Limits of the horizontal axis are different for the various panels.

Histograms of the parameter U_{peak} are reported in Figure 11 for both Phase 1 and Phase 3. Events with either positive or negative U_{peak} are embedded in the data sets, specifically with median values of −0.18 and −0.08 for Phase 1 and Phase 3, respectively. On the histograms of U_{peak} reported in Figure 11G and 11H, the vertical dashed lines indicate bins that will be used in the following to calculate the velocity profile statistics, which were selected to ensure sufficient statistical significance for the data related to Phase 3.

The conditional statistics of the velocity profiles measured by *PL*04 are calculated by using the above-mentioned bins of U_{peak} indicated with vertical dashed lines in Figure 11, both for Phase 1 and Phase 3. The binned statistics of the *PL*04 velocity profiles are reported in Figure 12 in terms of mean (lines) and intervals between the 25th and 75th percentile (shaded areas) for both Phase 1 (red) and Phase 3 (blue). For this figure, each measured velocity profile is made non-dimensional with U_∞, namely, the wind velocity measured at the highest location of 200 m. It is evident that these binned statics enable capturing the variability in wind shear for the site under investigation, ranging from large positive shear (bin center $U_{peak} = -0.3$ in Figure 12), to roughly zero shear (bin center $U_{peak} = -0.03$ in Figure 12), to large negative shear (bin center $U_{peak} = 1.2$ in Figure 12). A larger variability within each bin is observed for those characterized by $U_{peak} > 0$ (Figure 12), while the velocity profiles with $U_{peak} < 0$ are very similar. Regarding Figure 12, it is noteworthy that in general for each cluster, the statistics of the velocity profiles measured by the LiDAR *PL*04 are very similar for Phase 1 and Phase 3 of the experiment, especially for the clusters with negative values of U_{peak}. This feature indicates that no noticeable bias, such as wind seasonal variability, is present in the data sets collected before and after the construction of the turbine array under investigation.[35]

A similar statistical analysis based on U_{peak} is now performed for the instantaneous difference of the velocity profiles measured by the LiDARs *PL*04 and *PL*01, with the latter located 1.5*D* upstream of turbine *T*07 for the prevailing wind direction (see Figure 1A) and, thus, assumed within the induction zone. The velocity data are made non-dimensional with the turbine rated wind speed, U_{rated}, and the obtained results are shown in Figure 13. Starting from the wind conditions with $U_{peak} < 0$ (top row of Figure 13), it is evident that the mean profiles and the 25th to 75th percentile interval related to Phase 3 (blue symbols) generally indicate lower velocity values than their respective statistics for Phase 1 (red symbols). This feature might indicate a general velocity reduction over the rotor area due to the presence of the rotor of turbine *T*07. To separate the velocity difference that can occur between the locations of the LiDARs *PL*01 and *PL*04 due to topography for different climatological conditions and the velocity modification associated with turbine induction or wind farm blockage, the difference between Phase 3 and Phase 1 of the median profiles of the velocity difference between LiDAR *PL*01 and LiDAR *PL*04 is calculated for each bin and reported in Figure 14A (please note that in Figure 13 only the mean profiles are reported). This analysis shows a general velocity reduction occurring over rotor heights due to the installation

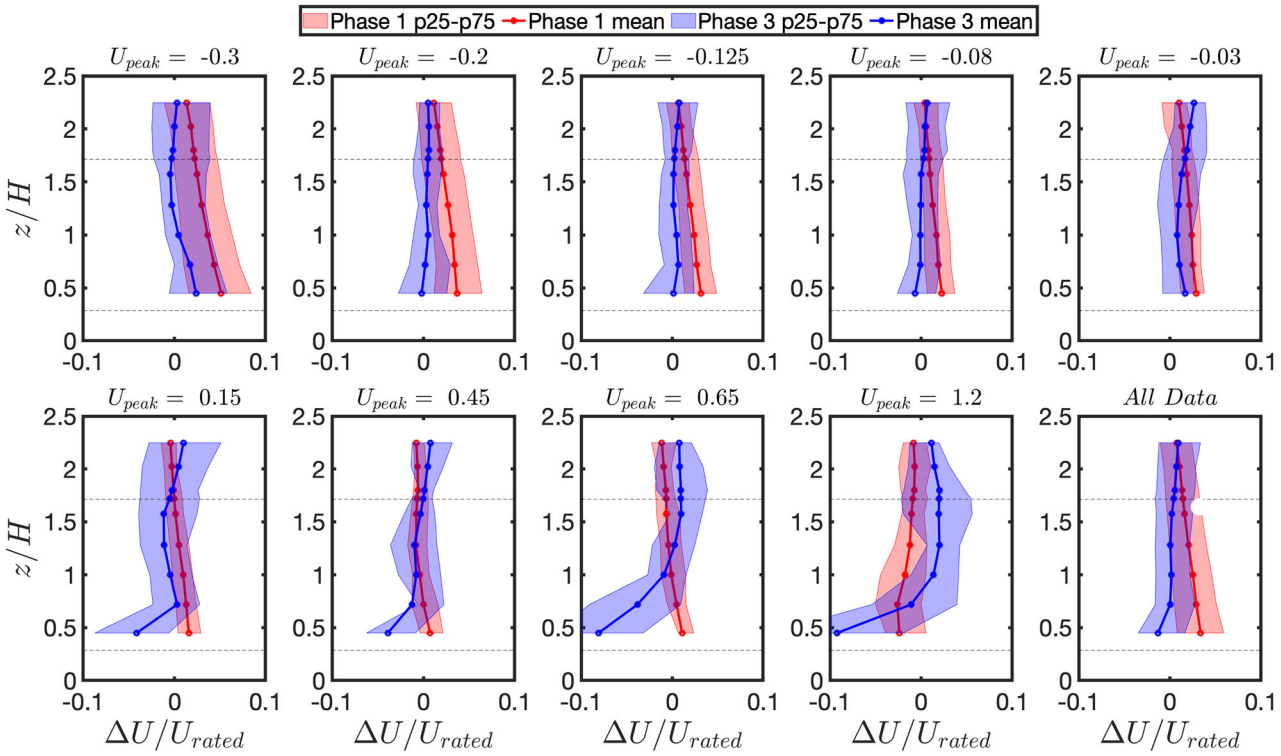

FIGURE 13 Binned statistics of the instantaneous difference between the velocity profiles measured by the LiDARs *PL*01 and *PL*04. Representations are analogous to those in Figure 12.

of the wind turbines. These velocity reductions range values between 3% and 1.3%, while they are more prominent over the top half of the rotor. These results are in general agreement with previous investigations on wind farm blockage.[13,16]

For the data bin corresponding to the mean velocity profile with the smallest shear ($U_{peak} = -0.03$ in Figure 14), besides the velocity reduction observed over the rotor heights, a slight velocity increase is observed above the rotor top tip ($z/H \approx 1.71$). It is noteworthy that this flow feature is also shared by the wind conditions characterized by $U_{peak} > 0$. Indeed, the difference of the median profiles between Phase 3 and Phase 1 data in Figure 14A shows that this velocity increase above the top tip is enhanced by increasing U_{peak}. Further, for wind conditions with $U_{peak} > 0$, a strong velocity decrease is measured below hub height, which increases with reducing height. Velocity reductions between -6% and -9% of the turbine rated wind speed are measured for the last two bins with the largest values of U_{peak}. On the other hand, a velocity increase is observed above hub height, with maximum values close to 3% of the turbine rated wind speed at the rotor top tip. Therefore, this analysis shows that rotor-induced effects on the incoming wind field are typically uniform across the rotor heights for wind conditions with positive wind shear, with typical values ranging from 3% down to 1% of the turbine rated wind speed with reducing shear. However, for incoming wind profiles with negative shear or low-level jet ($U_{peak} > 0$), the effects due to the rotor induction can be highly complex and, specifically, entailing significant velocity reductions in the lower half of the rotor with intensities increasing with reducing height, while speedups are observed on the upper half of the rotor.

An analogous binning analysis is now performed for the wind velocity data collected from the profiling LiDAR *PL*02, which is located at an upstream distance of about 3*D* from turbine *T*07 for the prevailing wind direction considered for this analysis, which is about twice the distance of the profiling LiDAR *PL*01. The statistics of the instantaneous difference of the profiles measured by the LiDAR *PL*02 and *PL*04 for Phase 1 (red) and Phase 3 (blue) data sets, which are reported in Figure 15, show that at this larger upstream distance from turbine *T*07, the velocity reduction is smaller than what was observed with the LiDAR *PL*01 at an upstream distance of 1.5*D*. For more quantitative analysis, the difference between the median profiles obtained from Figure 15 indicates that the velocity reduction over the rotor heights is practically negligible (Figure 14B). The only significant effect connected with the induction of the wind turbine rotors is detected for the two bins with the largest values of U_{peak}. Indeed, velocity reduction and increase are still observed below and above hub height, respectively, yet with a much lower magnitude (maximum around 1.5% of U_{rated}).

Finally, the same statistical analysis is performed for the data set collected by the profiling LiDAR *PL*03, which is located within the transverse area separating turbines *T*07 and *T*08 for the prevailing wind sector considered for this analysis (see Figure 1). The statistics from this LiDAR, reported in Figure 16, firstly indicate a larger variability within each bin with respect to the other LiDARs, and for several bins, the mean values reported with the dot-lines are significantly different from their respective median values, namely, the center of the 25th to 75th percentile interval (shaded areas). This suggests that this analysis might be more uncertain, especially for the data collected during Phase 1. This data variability might be associated with the mutual induction induced by both turbines *T*07 and *T*08, and their variability with wind direction and atmospheric

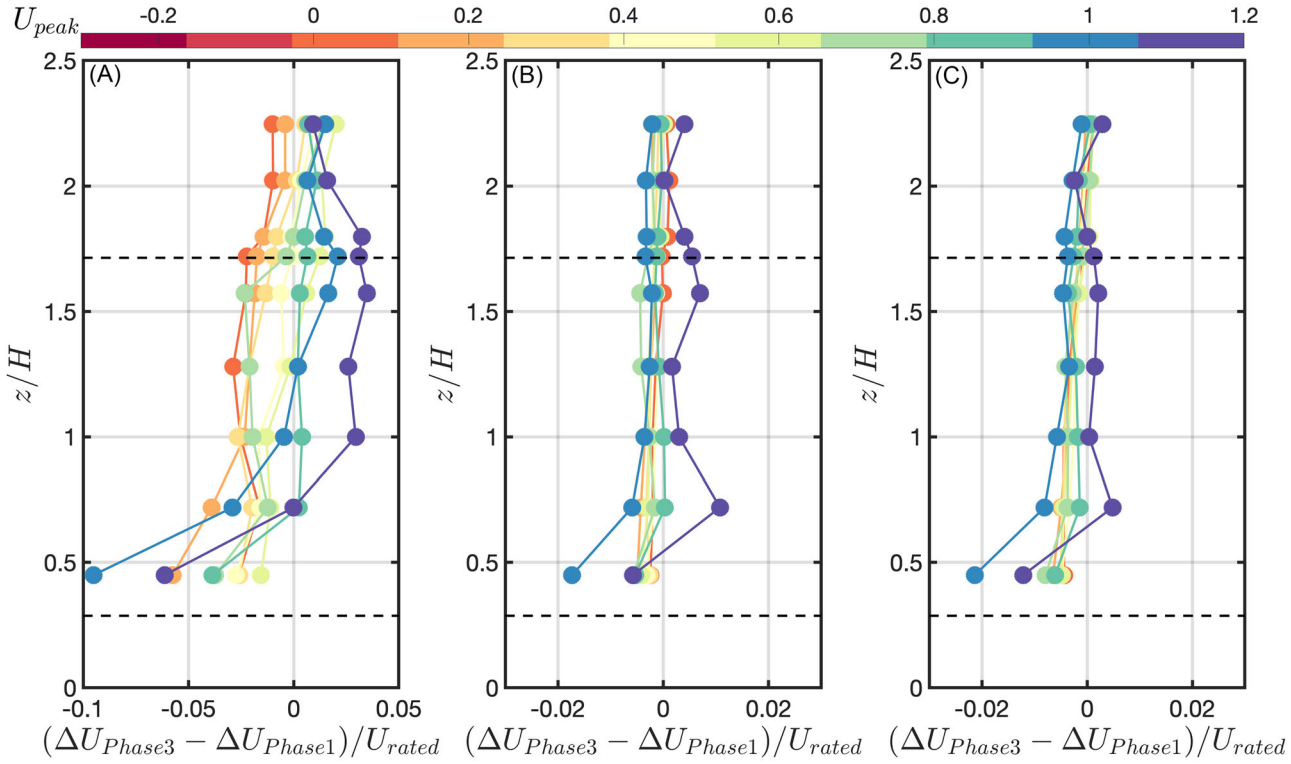

FIGURE 14 Difference of the median between Phase 3 and Phase 1 of the binned instantaneous difference between the velocity profiles measured by the LiDARs located in the proximity of the wind turbines and *PL*04: (A) Profiling wind LiDAR *PL*01; (B) profiling wind LiDAR *PL*02; (C) profiling wind LiDAR *PL*03.

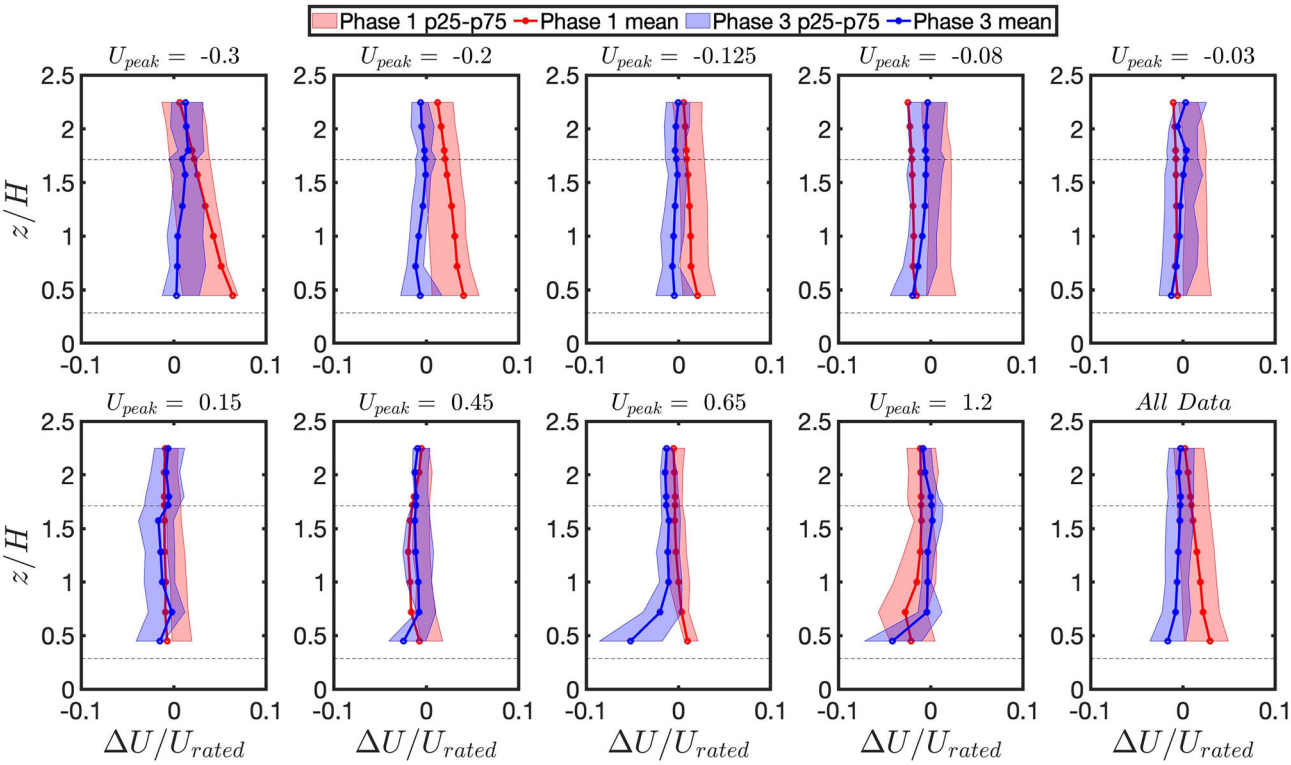

FIGURE 15 Binned statistics of the instantaneous difference between the velocity profiles measured by the LiDARs *PL*02 and *PL*04. Representations are analogous to those in Figure 12.

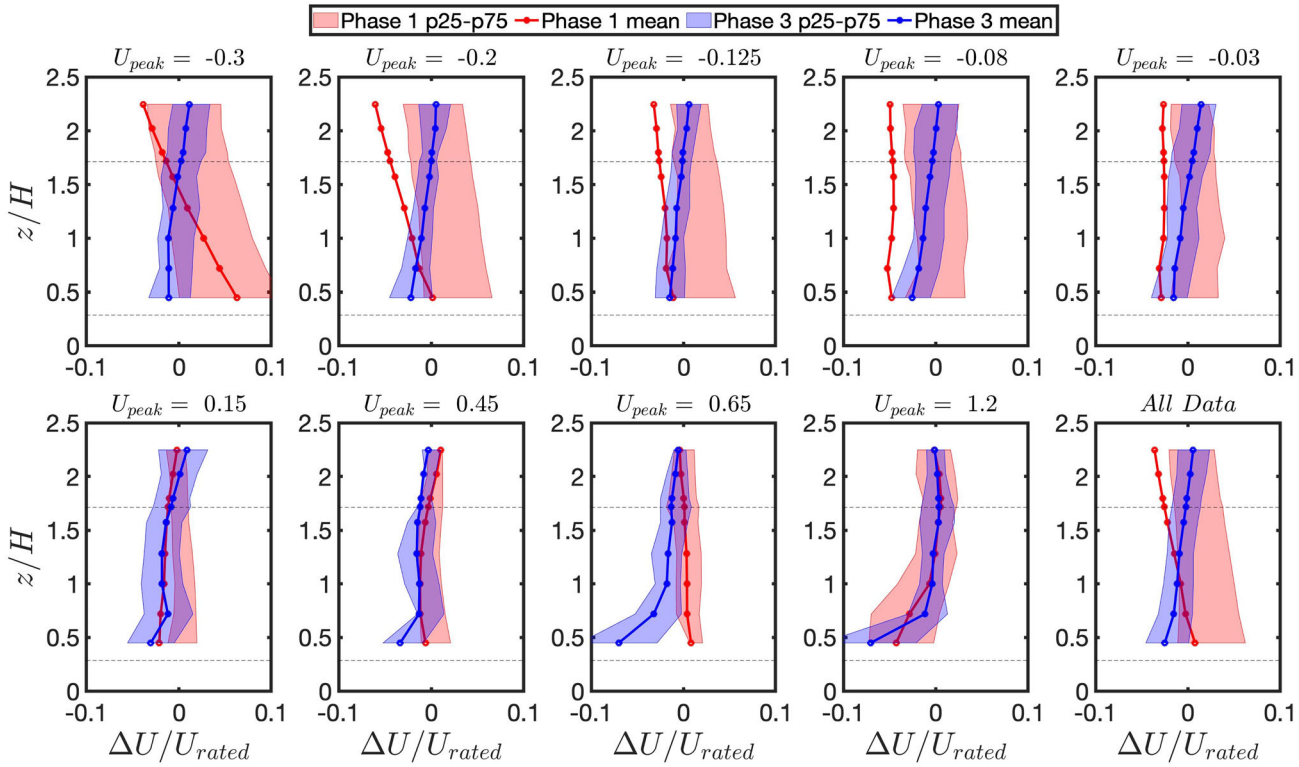

FIGURE 16 Binned statistics of the instantaneous difference between the velocity profiles measured by the LiDARs *PL*03 and *PL*04. Representations are analogous to those in Figure 12.

stability regime. Also at this position aside from the wind turbine rotors, the induction effects seem to be relatively small, with only significant effects for the more complex wind conditions with $U_{peak} > 0$ (Figure 14C).

5 | CONCLUSIONS

In this work, wind velocity measurements collected by four profiling wind LiDARs before and after the construction of an onshore wind turbine array have been analyzed to investigate rotor-induced effects on the incoming wind field. For the prevailing wind direction, the array mainly consists of a single row facing the incoming wind, with three profiling LiDARs located in front of the rotor of one of the turbines at the upstream distances of 1.5, 3, and 10 rotor diameters, *D*. The latter is regarded as a freestream unperturbed wind condition considering that at this location a maximum deviation from the freestream velocity of 0.4% was estimated through a modeling approach.[35] Another profiling wind LiDAR is located along the transverse distance between two consecutive wind turbines. SCADA data of the wind turbines are also available.

In the first part of the paper, the wind data collected by the most upstream profiling wind LiDAR have been interrogated to perform a climatology survey of the site under investigation. The study has been performed through a cluster analysis with the k-means algorithm and dendrogram approach, while the accuracy in the predictions of the wind climatology has been estimated through a random forest algorithm. This study has shown a good level of repeatability and predictability of the observed wind conditions with wind shear as a main driving wind parameter. This result is favorable to ensure the significance of the result obtained.

Besides expected wind conditions with different levels of positive shear, incoming wind profiles characterized by negative shear and low-level jet are also frequent for the site under investigation, specifically with occurrence rates of 14.5% and 1.4%, respectively, of the entire duration of the experiment. Furthermore, wind conditions with hub-height (89 m) wind speed smaller than 5 m/s are characterized by non-canonical wind profiles with large shear and/or veer with either positive or negative values. These conditions have been disregarded for further analysis.

The investigation of rotor-induced effects on the incoming wind field has been based on the analysis of the instantaneous difference of the incoming velocity profiles (measured at an upstream distance of about 10*D*, even though previous works showed that wind farm blockage might extend even up to 30*D* upstream[12]) and the velocity profile measured by the other three LiDARs located at streamwise distances of 1.5*D*, 3*D* and 10*D*, respectively, with the latter placed between two wind turbines. The variation of the difference in the velocity profiles measured by the upstream LiDAR characterizing the incoming wind velocity field and those measured by another LiDAR occurring between the pre- and post-

construction phases of the turbine array is investigated to separate effects due to the site topography for different climatological conditions and those associated with turbine induction and wind farm blockage.

Starting from the LiDAR located at an upstream distance of about 1.5*D*, velocity reductions up to 3% of the turbine rated wind speed have been quantified over the rotor heights for wind conditions with positive shear. The observed velocity reductions become smaller with reducing shear. For more unusual wind conditions with negative shear or low-level jet, a certain velocity increase is observed in the proximity of the top tip of the turbine rotor. This velocity increase is enhanced for wind conditions with more significant negative shear with values up to 3% of the turbine rated wind speed. For these wind conditions, increased velocity is measured over the top half of the turbine rotor, while velocity reduction is measured below, which is enhanced with reducing height (between −6% and −9%). Therefore, we infer that the rotor-induced effects for cases with negative shear and low-level jets are highly complex and consist of both velocity reductions and increases below and above hub height, respectively. These results suggest that more investigations should be needed to have a more detailed characterization of the velocity modifications induced by the wind turbine rotors for different operative conditions of the wind turbines and of the incoming wind, especially wind shear and, thus, atmospheric stability.

Data collected by the LiDAR located at an upstream distance of 3*D* have shown negligible effects associated with turbine rotor induction. The only noticeable effects are detected for wind conditions with negative shear, even if with a much smaller amplitude compared to the closer upstream location of 1.5*D*. Similar results have been obtained for the LiDAR located along the transverse direction between two turbines yet with larger statistical uncertainty due to the mutual inductions induced by the two wind turbines and their variability associated with variations of wind direction and atmospheric stability regime.

In summary, this study has provided evidence to confirm the occurrence of rotor-induced effects on the incoming wind field with typical values of about 3% of the turbine rated wind speed at an upstream distance of 1.5*D*. The rotor induction is more significant with increasing positive shear. For unusual wind conditions with negative shear or with the occurrence of low-level jets, these flow distortions are highly three-dimensional and become relatively complex. In this case, both velocity reduction and increase can be observed below and above hub height, respectively. It is noteworthy that, considering the small number of turbines comprised in the array under investigation, it is difficult to identify from the above-mentioned rotor-induced effects on the incoming wind the contribution associated with single-turbine induction from the cumulative effects due to wind farm blockage. Investigations for larger wind farms installed on different sites both onshore and offshore seem instrumental to enabling a more in-depth understanding of these wind farm phenomena.

This experiment has also provided the opportunity to confirm the extreme importance of the accuracy of the wind data collected, data quality control and down-selection, as well as the duration of the experiments to ensure a good statistical convergence of the data. Given the small magnitude of the flow modifications associated with wind farm blockage, the highly variable nature of the atmospheric wind field, and the variability of the wind turbine settings, field investigations of wind farm blockage are largely more challenging than other wind-turbine-related experiments, such as those related to wakes and power performance. It seems that synergistic work encompassing field experiments, laboratory experiments, and numerical simulations is going to be extremely beneficial in drawing a better picture of the physical processes associated with wind farm blockage, which is going to spur a breadth of future research activities.

ACKNOWLEDGEMENTS

This paper is based upon work partially supported by the National Science Foundation under grant numbers 1362022, 1362033, 1916715, and 1916776 (I/UCRC for Wind Energy, Science, Technology, and Research) and from the members of WindSTAR I/UCRC. Any opinions, findings, and conclusions or recommendations expressed in this material are those of the author(s) and do not necessarily reflect the views of the National Science Foundation or the sponsors. The authors are grateful to the Center for Wind Energy at UT Dallas for providing partial support for the publication costs. This material is partially supported by the National Science Foundation (NSF) CBET, Fluid Dynamics CAREER program, Award No. 2046160, program manager Ron Joslin.

PEER REVIEW

The peer review history for this article is available at https://www.webofscience.com/api/gateway/wos/peer-review/10.1002/we.2877.

DATA AVAILABILITY STATEMENT

The data that support the findings of this study are available from the corresponding author upon reasonable request.

ORCID

Coleman Moss https://orcid.org/0000-0002-4188-6915
Matteo Puccioni https://orcid.org/0000-0002-0764-9430
Giacomo Valerio Iungo https://orcid.org/0000-0002-0990-8133

REFERENCES

1. Medici D, Ivanell S, Dahlberg J, Alfredsson PH. The upstream flow of a wind turbine: blockage effect. *Wind Energy*. 2011;14(5):691-697.
2. Burton T, Jenkins N, Sharpe D, Bossanyi E. *Wind Energy Handbook*. John Wiley & Sons; 2011.
3. Branlard E, Quon E, Meyer Forsting AR, King J, Moriarty P. Wind farm blockage effects: comparison of different engineering models. *J Phys Conf Ser*. 2020;1618(6):62036.
4. Lanzilao L, Meyers J. Set-point optimization in wind farms to mitigate effects of flow blockage induced by gravity waves. *Wind Energ Sci*. 2021;6(1):247-271.
5. Sanchez Gomez M, Lundquist JK, Mirocha J, Arthur RS, Muñoz-Esparza D. Quantifying wind plant blockage under stable atmospheric conditions. *Wind Energ Sci Disc*. 2021;2021:1-21.
6. Letizia S, Moss C, Puccioni M, Jacquet C, Apgar D, Iungo GV. Effects of the thrust force induced by wind turbine rotors on the incoming wind field: a wind LiDAR experiment. *J Phys: Conf Ser*. 2022;2265(2):22033.
7. Nishino T, Willden RHJ. The efficiency of an array of tidal turbines partially blocking a wide channel. *J Fluid Mech*. 2012;708:596-606.
8. McTavish S, Rodrigue S, Feszty D. An investigation of in-field blockage effects in closely spaced lateral wind farm configurations. *Wind Energy*. 2014;18:1989-2011.
9. Nishino T, Draper S. Local blockage effect for wind turbines. *J Phys: Conf Ser*. 2015;625(1):12010.
10. Meyer Forsting AR, Troldborg N, Gaunaa M. The flow upstream of a row of aligned wind turbine rotors and its effect on power production. *Wind Energy*. 2017;20:63-77.
11. Sebastiani A, Castellani F, Crasto G, Segalini A. Data analysis and simulation of the Lillgrund wind farm. *Wind Energy*. 2021;24(6):634-648.
12. Schneemann J, Theuer F, Rott A, Dörenkämper M, Kühn M. Offshore wind farm global blockage measured with scanning LiDAR. *Wind Energy Sci*. 2021;6:521-538.
13. Bleeg J, Purcell M, Ruisi R, Traiger E. Wind farm blockage and the consequences of neglecting its impact on energy production. *Energies*. 2018;11(6):1609.
14. Wu KL, Porté-Agel F. Flow adjustment inside and around large finite-size wind farms. *Energies*. 2164;10(12):2017.
15. Centurelli G, Vollmer L, Schmidt J, Dörenkämper M, Schröder M, Lukassen LJ, Peinke J. Evaluating global blockage engineering parametrizations with LES. *J Phys: Conf Ser*. 2021;1934(1):12021.
16. Bleeg J, Montavon C. Blockage effects in a single row of wind turbines. *J Phys: Conf Ser*. 2022;2265(2):22001.
17. Ebenhoch R, Muro B, Dahlberg JÅ, Berkesten Hägglund P, Segalini A. A linearized numerical model of wind-farm flows. *Wind Energy*. 2017;20(5):859-875.
18. Segalini A, Dahlberg J. Blockage effects in wind farms. *Wind Energy*. 2020;23(2):120-128.
19. Letizia S, Zhan L, Iungo GV. LiSBOA (LiDAR Statistical Barnes Objective Analysis) for optimal design of LiDAR scans and retrieval of wind statistics - Part 1: Theoretical framework. *Atmos Meas Tech*. 2021;14(3):2065-2093.
20. Letizia S, Zhan L, Iungo GV. LiSBOA (LiDAR Statistical Barnes Objective Analysis) for optimal design of LiDAR scans and retrieval of wind statistics - Part 2: Applications to LiDAR measurements of wind turbine wakes. *Atmos Meas Tech*. 2021;14(3):2095-2113.
21. Puccioni M, Calaf M, Pardyjak ER, Hoch S, Morrison TJ, Perelet A, Iungo GV. Identification of the energy contributions associated with wall-attached eddies and very-large-scale motions in the near-neutral atmospheric surface layer through wind LiDAR measurements. *J Fluid Mech*. 2023;955:A39.
22. Renganathan SA, Maulik R, Letizia S, Iungo GV. Data-driven wind turbine wake modeling via probabilistic machine learning. *Neural Comp Appl*. 2022;34(8):6171-6186.
23. Iungo GV, Maulik R, Renganathan SA, Letizia S. Machine-learning identification of the variability of mean velocity and turbulence intensity for wakes generated by onshore wind turbines: cluster analysis of wind LiDAR measurements. *J Ren Sust Energ*. 2022;14:23307.
24. Letizia S, Iungo GV. Pseudo-2D RANS: a LiDAR-driven mid-fidelity model for simulations of wind farm flows. *J Ren Sust Energ*. 2022;14:23301.
25. Jain AK, Murty MN, Flynn PJ. Data clustering: a review. *ACM Comput Surv (CSUR)*. 1999;31(3):264-323.
26. Breiman L. Random forests. *Mach Learn*. 2001;45(1):5-32.
27. Biau G, Scornet E. A random forest guided tour. *Test*. 2016;25(2):197-227.
28. Smith CM, Barthelmie RJ, Pryor SC. In situ observations of the influence of a large onshore wind farm on near-surface temperature, turbulence intensity and wind speed profiles. *Environ Res Lett*. 2013;3:34006.
29. Iungo GV, Porté-Agel F. Volumetric LiDAR scanning of wind turbine wakes under convective and neutral atmospheric stability regimes. *J Atmos Ocean Tech*. 2014;31:2035-2048.
30. El-Asha S, Zhan L, Iungo GV. Quantification of power losses due to wind turbine wake interactions through SCADA, meteorological and wind LiDAR data. *Wind Energy*. 2017;11:1823-1839.
31. Forina M, Armanino C, Raggio V. Clustering with dendrograms on interpretation variables. *Anal Chim Acta*. 2002;454(1):13-19.
32. Rousseeuw PJ. Silhouettes: a graphical aid to the interpretation and validation of cluster analysis. *J Compt Appl Math*. 1987;20:53-65.
33. Pedregosa F, Varoquaux G, Gramfort A, et al. Scikit-learn: machine learning in Python. *JMLR*. 2011;12:2825-2830.
34. Zhan L, Letizia S, Iungo GV. Optimal tuning of engineering wake models through LiDAR measurements. *Wind Energ Sci*. 2020;5(4):1601-1622.
35. Jacquet C, Apgar D, Chauchan V, Storey R, Kern S, Davoust S. OFarm blockage model validation using pre and post construction LiDAR measurements. *J Phys: Conf Series*. 2022;2265(2):22009.

How to cite this article: Moss C, Puccioni M, Maulik R, Jacquet C, Apgar D, Valerio Iungo G. Profiling wind LiDAR measurements to quantify blockage for onshore wind turbines. *Wind Energy*. 2023;1-18. doi:10.1002/we.2877